Optical Fiber Pressure Sensors for Adaptive Wings

Paul G. Duncan, Mark E. Jones, Kevin A. Shinpaugh, and Stephen H. Poland
F&S, Inc., 2801 Commerce Street, S.E., Blacksburg, VA 24060

Kent A. Murphy and Richard O. Claus
Fiber & Electro-Optics Research Center, Bradley Department of Electrical Engineering
Virginia Tech, Blacksburg, VA 24061-0356

ABSTRACT

Optical fiber pressure sensors have been developed for use on a structurally-adaptive "smart wing"; further details of the design, fabrication and testing of the smart wing concept are presented in companion papers. This paper describes the design, construction, and performance of the pressure sensor and a combined optical and electronic signal processing system implemented to permit the measurement of a large number of sensors distributed over the control surfaces of a wing.

Optical fiber pressure sensors were implemented due to anticipated large electromagnetic interference (EMI) signals within the operational environment. The sensors utilized the principle of the extrinsic Fabry-Perot interferometer (EFPI) already developed for the measurement of strain and temperature. Here, the cavity is created inside a micromachined hollow-core tube with a silicon diaphragm at one end. The operation of the sensor is similar to that of the EFPI strain gage also discussed in several papers at this conference. The limitations placed upon the performance of the digital signal processing (DSP) system were determined by the required pressure range of the sensors and the cycle time of the control system used to adaptively modify the shape of the wing. Sensor calibration and the results of testing performed are detailed.

Keywords: pressure transducers, fiber optic sensors, smart wing, instrumentation

1. INTRODUCTION

With the development of modern aerospace and high energy applications new requirements have emerged for existing measurement technologies. Long established methods of measurement, once considered irrefutable, are being continually pushed to their limits due to expanding technologies. Of particular interest with respect to measurement and measurement technique are flight dynamics and the visualization of flow fields across control surfaces. Advances in composite and smart structure technologies have led to embedded, lightweight sensors working simultaneously with actuation systems to provide a response and correction to environmental perturbations. Maturation of this research area is necessary to develop technologies needed for future smart aircraft that are able to sense airflow across the surface of wings and then respond to these perturbations with adjustments in attack angle and wing shape. Specific improvements attributable to this new capability include higher speeds, enhanced aircraft maneuverability, increased payload sizes, greater range, reduced vibration and flutter, increased aircraft safety, reduced fuel consumption, and reduced noise pollution, to name a few.

Programs are currently underway that will culminate in the development and wind tunnel testing of an integrated wing with a sensing/actuation system – specifically, the DARPA Smart Wing program led by Northrop-Grumman Corporation. The nature of this program has established measurement environments considered too harsh for conventional measurement methods and has resulted in the development and application of fiber optic strain and pressure sensors.

Optical fiber sensors are required for pressure sensor implementation within shape memory alloy (SMA) control structures due to several reasons: (1) weight concerns attributed to potentially hundreds of sensor arrays, (2) the level of anticipated EMI which occurs as a result of the control currents through the SMA actuators, and (3) the anticipated long distances between the actual sensing point and instrumentation electronics. The all-dielectric nature of optical fiber data networks and sensor instrumentation systems implies a greatly improved signal-to-noise ratio and a natural immunity to transient signal interference or potential jamming. Furthermore, the light weight of optical fibers is essential for fly-by-light applications. This paper describes a fiber optic pressure instrumentation system and a robust differential pressure sensor developed specifically for aerospace applications. Additionally, pressure data collected in NASA Langley's Transonic Dynamics Tunnel (TDT) using a scale F/A-18 wing is presented.

SPIE Vol. 3042 • 0277-786X/97/$10.00

2. FIBER OPTIC PRESSURE SYSTEM OVERVIEW

The major components which comprised the fiber optic pressure system were the following: (1) the fiber optic sensors, (2) the fiber trunk line, (3) the excitation and demodulation electronics, and (4) the data acquisition system.

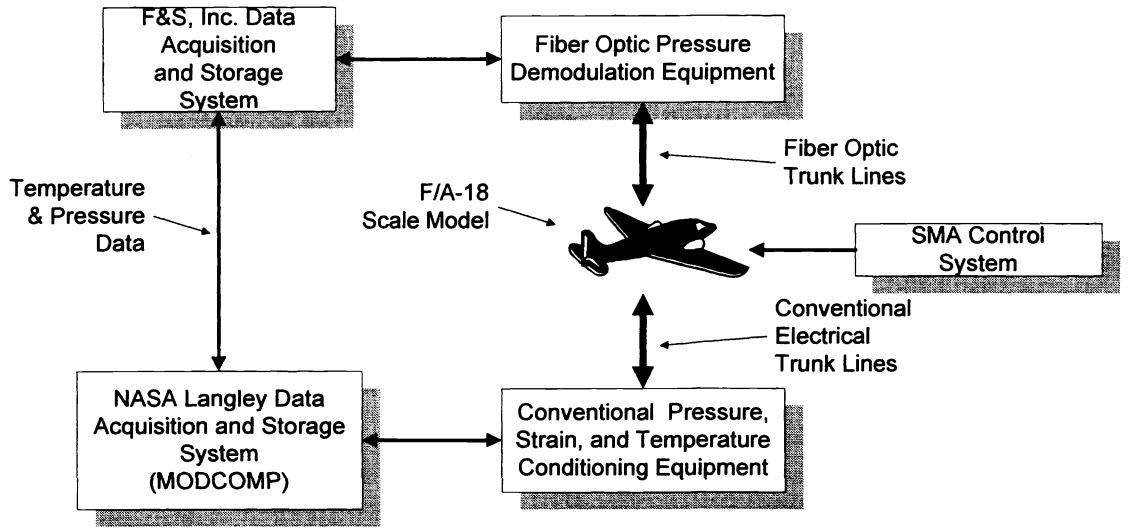

Figure 1. Major components of the fiber optic smart wing (SWING) system.

Discussed in other papers at this conference are (1) the test article, a F/A-18 1/6th scale wing model, (2) the conventional sensor network installed in the model, (3) NASA Langley's extensive data acquisition system – the MODCOMP, and (4) the SMA control system. Figure 1 shows the relationship between these components.

The fiber optic pressure demodulation and data storage system developed for this program is shown in Figure 2. The key components are (1) ten fiber optic pressure sensors, (2) ten fiber optic trunk lines, (3) ten fiber optic pressure

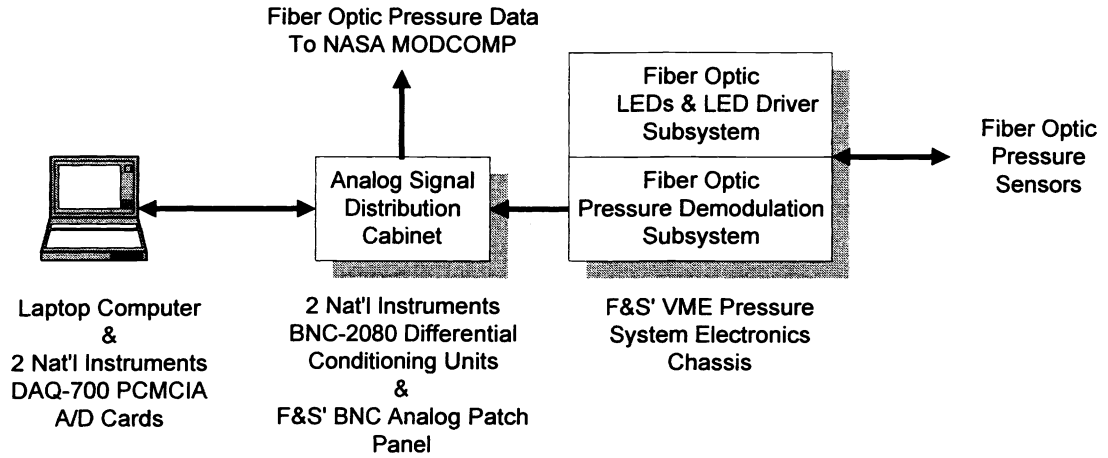

Figure 2. Key components of the fiber optic pressure demodulation and data storage system.

demodulation channels, (4) a sixteen channel signal distribution cabinet, and (5) a laptop PC data acquisition and storage system using PCMCIA cards.

The VME electronics system which was developed for this program contained all electronics necessary for generating the required signals to interrogate the fiber optic sensors as well as processing the return signals. A top-level explanation of the system is as follows. The front end of the VME system contains the broadband LEDs which was used to

excite the fiber optic pressure sensors. Through wavelength-flattened fiber optic coupler arrays five LED sources were launched down ten bend-insensitive (BI) fiber optic trunk lines. Spliced to the end of each trunk line was a fiber optic pressure sensor which operated using the same principle as the EFPI. The pressure intensity modulated the LED signal which was returned down the same incident path and was demodulated by the VME rack assembly.

After processing, the output of the VME system was a linearized voltage corresponding to the pressure sensor signal – this voltage signal was routed to an analog distribution cabinet. The sensor outputs from the VME were differentially configured and thus the data acquisition system was designed as a differential processing system. This task was made easy through the implementation of two National Instrument's BNC-2080 patch panels which convert an incoming signal on a BNC connector into two separate channels. As such, 20 data acquisition channels were required to record ten fiber optic channels. Data acquisition was accomplished on a laptop computer which contained two National Instrument's DAQ-700 12-bit analog to digital converter cards. Each of these cards, configured via software for differential mode, provided up to eight channels of differential data acquisition. Additionally, fiber optic pressure data was also made available to NASA's MODCOMP computer system for storage and subsequent analysis.

3. DETAILED DESCRIPTION

3.1 Fiber optic pressure sensor design

The design of the optical fiber pressure transducer, based upon an EFPI as shown in Figure 3, relies on the movement of a flexible diaphragm to modulate the interferometric cavity. Deflection of the diaphragm is governed

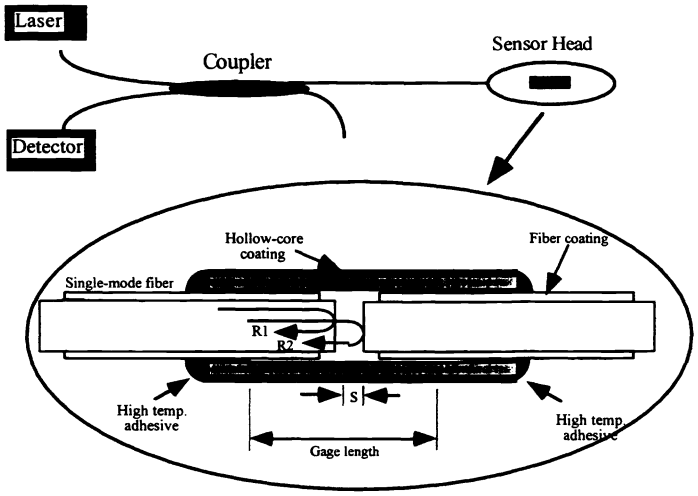

Figure 3. Schematic of the extrinsic Fabry-Perot Interferometer (EFPI).

approximately by[1]

$$Y = \frac{3(1-\nu^2)Pa^4}{16ET^3} \tag{1}$$

where Y is the distance of deflection, E is the modulus of elasticity, ν is Poisson's ratio, T is the diaphragm thickness, and a is the radius. The basic sensor consists of a lead-in, single-mode fiber and a reflecting diaphragm held in alignment with a specially designed ferrule.

With reference to Figure 3 the two reflections, R_1 and R_2, originate at each air/glass interface and travel back through a 2 x 2 coupler where the intensity fringes resulting from their interference are monitored by a low-noise photodetector. The output of the sensor is described by the equation[2]

$$I_{det} = A^2((1+\frac{2ta}{a+2s\tan(\sin^{-1}(NA))}\cos(\frac{4\pi s}{\lambda}))+(\frac{ta}{a+2s\tan(\sin^{-1}(NA)}))^2) \quad (2)$$

where A is the amplitude of the input signal, a is the fiber core radius, t is the transmission coefficient of the air-glass interface (~0.96), s is the end separation, NA is the numerical aperture of the single-mode fiber, given by $NA=(n_1^2 - n_2^2)^{1/2}$, and n_1 and n_2 are the refractive indices of the core and the cladding, respectively. This system used a high power, broadband LED which had a coherence length of approximately 25 μm. The sensors were constructed to operate outside of the coherence length of the source which caused the change in intensity of the envelope function of Equation (2) to be the determining measurement criteria, not the individual phase interaction between R_1 and R_2 in the interferometer.

The design of the optical fiber pressure transducer is shown in Figure 4. The diaphragm and housing were supplied by Pressure Systems Incorporated (PSI) of Hampton, Virginia. The silicon micromachined diaphragm was mounted on a Pyrex substrate with a hole at the back of the diaphragm to allow alignment of the optical fiber. A strain relief and alignment ferrule was fabricated out of Invar and included vent holes allowing access to the back of the diaphragm. Positioning of the fiber with respect to the diaphragm was accomplished actively using precise three-axis micropositioners. During alignment, the front of the diaphragm was pressurized. Maximum deflection occurred at the center of the diaphragm and the optical fiber was aligned for maximum returned intensity. The initial gap of the sensor was set using F&S' absolute fiber support system (AFSS) which allowed setting of the gap to within tens of nanometers of the desired gap.

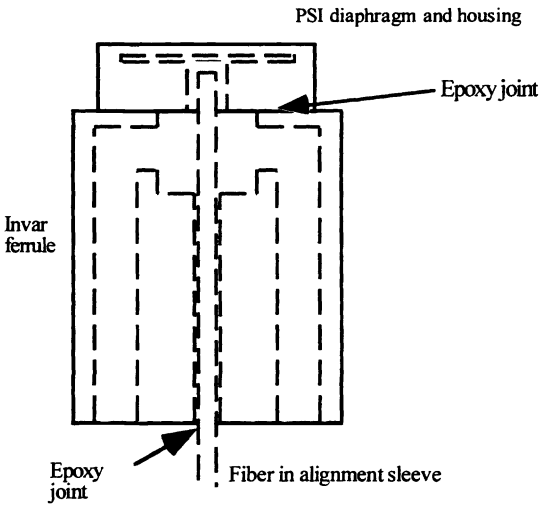

Figure 4. Diagram of PSI pressure housing mounted on an Invar ferrule.

3.2 Electro-optical design

An industry standard VME 6U card assembly was developed for this program which contained the integrated optical and electronic subassemblies. These cards were inserted into a standard 19" VME rack assembly to comprise a ten-channel pressure system. A second rack assembly consisting of six additional channels was also built to provide additional strain or pressure channels if the need arose.

The next figure shows the electro-optical cabinet and analog interface patch panel; the various subsystems of the VME cabinet are detailed below.

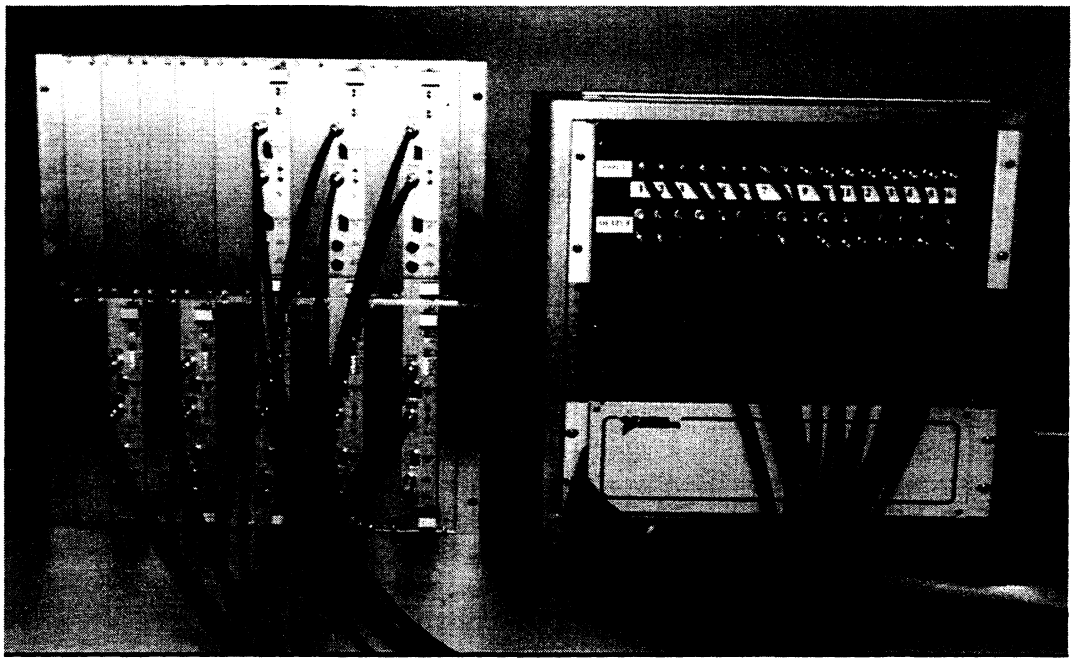

Figure 5. Front panel view of the VME fiber optic pressure system and the analog signal distribution cabinet. Sixteen channels were developed for this project.

3.2.1 Optical system configuration

Figure 6 details the configuration of the optics subsystem. Two distinct optical paths from the LED source to the individual sensors are shown – this was the final configuration as designed and installed on one VME circuit card assembly. As a result five VME cards were necessary to complete the ten channel requirement. Note that through the use of higher power sources it would be possible to extend this same topology to a four channel configuration (one source, seven couplers) which would allow for even greater channel densities within a standard 19" VME rack.

Also indicated in Figure 6 are blocks which represent the LED driver and stabilization circuitry – the LED driver is a closed-loop constant optical power system which is necessary in most intensity modulation processes. Optical energy generated by the driver and LED was launched into standard single mode optical fiber (SMOF) and was split into two equal amounts by the first fiber optic coupler. Due to operation outside of the coherence length of the source, back reflections caused by the couplers, fusion splices, connectors, and sensors did not substantially effect the optical power stability of the source which precluded using an inline optical isolator between the source and the first coupler. The energy in each of these fiber coupler arms was again split 50/50 in the second chain of couplers and subsequently passed to the respective channel sensor and/or driver reference circuit. Incident energy upon the driver reference circuit was used to develop an error signal which adjusted the output energy of the LED. If a decrease in forward power was sensed in the driver reference circuit this caused an error signal to drive the LED harder; similarly an increase in power would correspond to a command to decrease driver current. Stability of greater than 70 ppm in forward optical power was typical.

[A note concerning a characteristic of this constant power system which is different than most commercially available controller circuits. Many LED controller circuits rely upon the use of a back facet monitor (BFM) which is a photodiode connected directly to the semiconductor LED or LASER (L/L) substrate. The BFM provides a direct method to monitor the optical power within the L/L. Unfortunately, the BFM gives no indication as to the throughput power (i.e., power coupled into the SMOF) so using only an integrated BFM/LED assembly for intensity demodulation will yield poor results. Experimentally it was discovered that the power coupled into the SMOF from the LED varied greatly as a function of temperature of the L/L assembly; using an external photodiode to sense these power fluctuations provided a system stability increase of two orders of magnitude.]

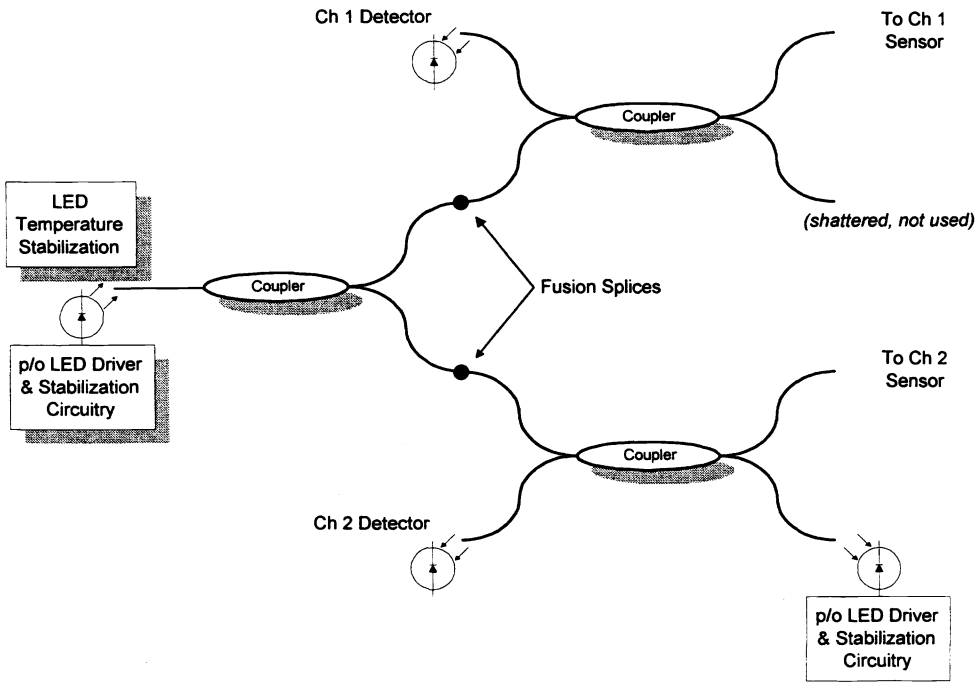

Figure 6. VME card two-channel optical configuration.

Finally, in order to further increase the intensity stability of the system LEDs were selected which were mounted upon a Peltier (a thermoelectric cooler) and were connected to standard temperature bridge control circuitry. Each LED contained a thermistor which provided the localized feedback temperature necessary to maintain the LED substrate at a constant temperature. Keeping the LED at a constant temperature maintained thermal efficiency which resulted in additional power stability (> 20 ppm forward power).

3.2.2 Optical power stability design

This next section describes the topology of the LED driver and output power stabilization electronics. Refer to Figure 7 as necessary. An extremely low-noise, temperature stable voltage reference established the quiescent current level

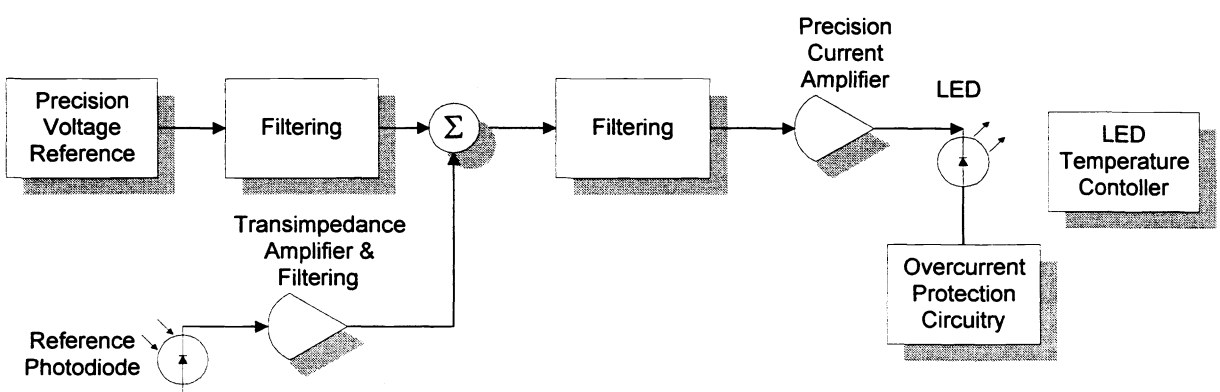

Figure 7. LED driver and power stabilization block diagram.

to drive the output LED. This DC signal was filtered to remove the high frequency noise associated with voltage references and was applied to a summation error amplifier. The other input to this error amplifier was from the reference photodiode circuitry which continuously monitored the forward power in the system (refer to Figure 6). The output from the error circuitry was filtered again to remove higher frequency noise components and then applied to a precision transconductance circuit. The drive current through the LED was monitored at all times by over-current protection circuitry to prevent destruction of the LED in the event of an optical harness failure (loss of reference photodiode input). Additionally, a standard four-legged precision bridge temperature controller was designed which stabilized the LED substrate temperature to approximately 20°C ± 0.1°C (ambient was typically at 27°C).

3.2.3 Optical transmission

Although the test article was less than 15m from the instrumentation equipment approximately 75m x 16 (16 channels were built) of fiber optic trunk lines were required to convey the optical pressure data to the demodulation system. Due to anticipated vibrations within the TDT while running at transonic speeds SMOF which was bend insensitive (BI) was run from the model to the TDT control room. This BI fiber was relatively immune to macro bending losses caused by installation and provided extremely clean optical signals to the demodulation system.

3.2.4 Pressure sensor demodulation input design

The return signal from the pressure sensor was applied to the front-end circuitry shown in Figure 8. The front end of the demodulation system is comprised of (1) the input photodiode which receives the raw fiber optic pressure signal, (2) a transimpedance amplifier which converts the photodiode current signal into a proportional voltage signal, (3) an offset circuit which removes DC bias current from the input photodiode, (4) an anti-aliasing filter network to remove any frequency component of the pressure signal that could be above the Nyquist frequency, (5) a precision 16-bit analog to digital (A/D) converter, and (6) a digital signal processor (DSP) which performed timing, control, and data manipulation functions.

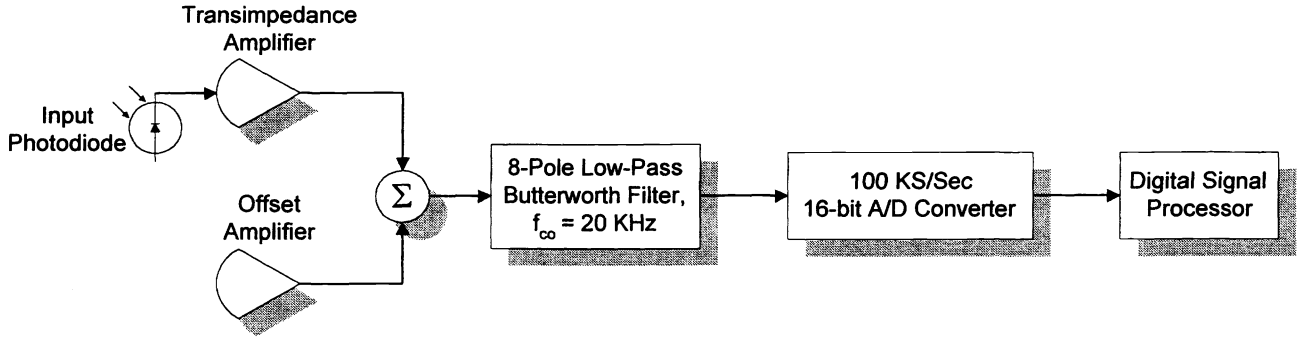

Figure 8. Pressure sensor demodulation front end topology.

3.2.5 Signal processing and calibration

The signal processing involved for an intensity based sensor relies heavily upon known parameters which are determined by each modulation/demodulation (mod/demod) channel. These parameters can be separated into two groups – system and sensor. System parameters are measurable characteristics which are accounted for in the calibration process and include the LED power transfer function, optical harness losses (coupling ratios, fusion splicing, connectorization issues, etc.), and photodiode responsivities. Sensor parameters are characteristics which are defined in the sensor manufacturing process and include sensitivity to the desired measurand, initial gap determination, and consistent, repeatable manufacturing practices. By classifying characteristics in this manner complex algorithms were developed which allowed on-site initialization and calibration of the sensors with minimal effort.

System parameters varied channel to channel and had to be accounted for in the system calibration process. Specifically, LED power directly affected the signal to noise ratio (SNR) of the demodulation system. Through the use of high-gain transimpedance amplifiers SNR was increased, but only to a point due to amplifier gain bandwidth constraints and open loop noise gain limitations. This section of the front end demodulators controlled the numeric values of curve-fitting

coefficients used in the runtime algorithms. As designed the channels could withstand considerable attenuation (1 ~ 2 dB) due to connectorization losses and still be accurate to 1% full scale which exceeded initial design goals of 5% full-scale accuracy.

During calibration of each sensor a known pressure using PSI's Model 9010 pressure calibrator was applied to the pressure sensor and the corresponding 16 bit A/D value was read into the DSP. This automated process was repeated several times, the values averaged, and a corresponding short look-up table was constructed. This table was then input into another algorithm which curve fit the values using a standard least-squares routine and a corresponding 16 bit (65,536 state) lookup table was generated. This table, unique to the particular sensor being calibrated, was loaded into flash EEPROM on the DSP board to be saved for runtime operations. Thus, a sensor became dedicated to a particular mod/demod channel.

The initial state of a particular channel could not be standardized due to differences in individual sensor installation at NASA's TDT and as a result a method had to be developed which would allow easy, repeatable initialization of the sensors. A reset sequence was established which, when initiated, oversampled the A/D value and stored this as an initial condition. This oversampled value became the point to which the output circuitry was referenced – a pressure equal to the initial starting pressure would correspond to a 0-volt output. Algorithmically this initial condition, when combined with channel parameters, became an offset value for the lookup table.

Runtime operations were straight forward. The A/D sampled the photodetector and sent this value to the DSP. After scaling and curve fitting this value an index in a 16-bit lookup table was generated. This lookup table value was sent to a digital to analog converter section (described below) where full-scale corresponded to a pressure from -5 to +5 psi_d.

3.2.6 Pressure sensor demodulation output design

Figure 9 depicts the single channel output configuration of each mod/demod card. The DSP, after determining the correct pressure level, sent a 16 bit word to a digital to analog (D/A) converter. The D/A converter output a value which was filtered and scaled by the output scaling amplifier and buffers. The result was a ±10v full-scale output which corresponded to ±5 psi_d. The output was kept "floating" in anticipation of a potentially corrupted building ground – this method allowed for true differential measurement of the output signal and high common mode rejection of 60 Hz ground currents.

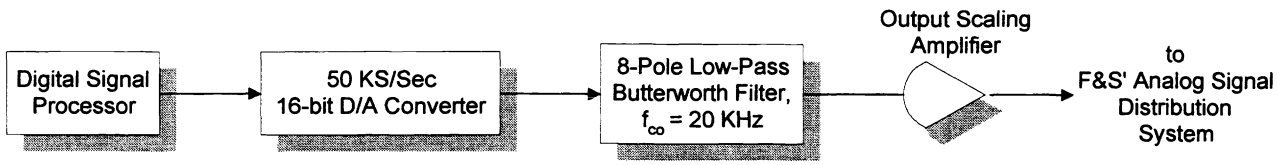

Figure 9. Pressure sensor demodulation output section topology.

3.3 Signal Interfacing

In order to preserve the differential output configuration of the fiber demodulation system F&S built a differential patch panel which interfaced directly with a laptop PC containing two National Instruments PCMCIA DAQ-700 cards. Each card provides for 16 single ended (all referenced to the same point) or eight differentially ended inputs (no common reference). Sixteen optical channels were built although only ten were expected to be in use at any given time – this mandated that two DAQ-700 cards be used for data collection.

NASA's MODCOMP data acquisition system used high impedance differential inputs on each of its channels so directly connecting F&S' output pressure signal to both acquisition systems resulted in no problems. Also note that temperature data processed through the MODCOMP was not directly acquired and stored by F&S. NASA provided data files which were integrated with F&S' data records to correlate pressure and temperature.

4. TEST DESCRIPTION

Testing took place in May of 1996 at NASA Langley's TDT. Specifics involving the test matrix, instrumentation, and results have been presented in other papers at this conference by Northrop-Grumman. With respect to F&S ten fiber optic pressure sensors were installed and proper operation verified in the test article. Each F&S pressure sensor was co-

located with a conventional PSI pressure sensor in order to provide correlated data. Each F&S fiber optic sensor was also instrumented with a conventional thermocouple so that temperature effects upon the fiber sensors could be determined.

Each sequence of tests which were conducted on the wing were done so at varying air speeds, different angles of attack, different flap conditions, etc. Each condition was set according to the test matrix; the data were captured and then the next adjustment to the model was made. In each case F&S and NASA captured data simultaneously such that the temperature and pressure data reported by NASA corresponded temporally with F&S' data. In all, several weeks of data were collected by NASA, Northrop-Grumman, and F&S.

5. RESULTS

By the end of the test sequence seven of the ten fiber optic sensors remained fully operational. Unfortunately, early in the test sequence fiber optic pressure sensor 2 failed to provide any output and sensors 5 and 10 became suspect in what they reported. Likely failure modes for these sensors were (1) tight bend radii imparted on each fiber lead-in due to its physical placement within the model and (2) the cramped conditions surrounding each sensor due to other instrumentation and control interfacing systems. Figure 10 details the physical locations of the fiber optic sensors – note that the wing gets markedly thinner as the distance from the root increases which contributed to the bending losses in sensors 2, 5, and 10. The first number in the sensor designation in Figure 10 is the fiber optic pressure number, the second value is either a "T" or a "B" and represents whether the sensor was monitoring the top or bottom surface. The last three alphanumeric characters represent the conventional pressure channel as designated by Northrop-Grumman. For example, 6T/B16 is the channel 6 fiber optic sensor, monitoring the top surface, and co-located with Northrop-Grumman sensor B16.

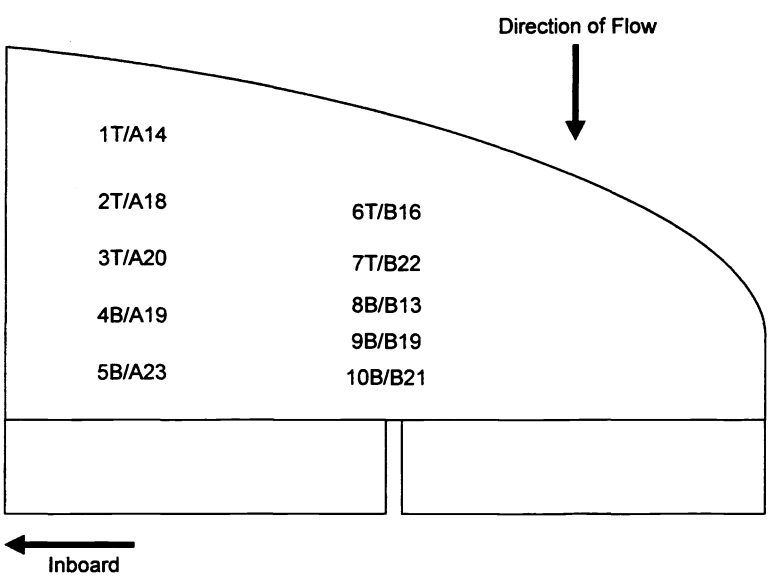

Figure 10. Top view of wing showing the relative locations of the fiber optic pressure sensors.

F&S instrumented all ten fiber optic pressure sensors with conventional thermocouples – this forethought proved invaluable due to a demonstrated dependence on temperature changes. This dependency contradicted laboratory results – a 70°C change in ambient temperature typically produced less than 5% change in optical output signal. Standard temperature changes in the TDT were on the order of 15°C differential and this produced an average 10% change in the pressure signal.

5.1 Data analysis

In order to decouple the effects of temperature on the fiber pressure measurements data had to be compiled with F&S' data records from NASA's MODCOMP data acquisition system. NASA's records provided localized temperature for the fiber optic sensors, angle of attack information, free-stream velocity, tunnel pressure, wing pressure, and (conveniently) F&S' fiber optic pressure. A multiple linear regression[3] was performed on each variable with respect to fiber pressure and coefficient of determination (R^2) values were attained. Ranking the coefficients from greatest dependency to least revealed the following order:

- temperature
- angle of attack
- stream velocity
- tunnel pressure

Based upon these findings a set of equations were developed to remove the temperature dependency in our data. Figure 11 reveals the results for tunnel runs 39 through 55 (approximately 550 data sets). Channel 2 has been omitted due to the detected failure of the optics path early in the test sequence. The x-axis corresponds to the sensor number and the y-axis to pressure error as compared to the NASA pressure recordings. Four plots are shown, two corresponding to data with no temperature correction and the other two with temperature correction. The mean error values are literally that – the error between Northrop-Grumman's (NG) pressure sensor and F&S' pressure sensor was determined for all data sets examined. The standard error was calculated on a smaller set of data to determine variability in data sets – the closer the standard error value is to the mean error the more statistically reliable our analysis.

Referring to Figure 11 we see that sensors 1, 4, 6, 7, and 8 had mean and standard errors of less than 0.075 psi. These sensors, in addition to sensor 3 all exhibited low variance between the temperature corrected and the non-corrected

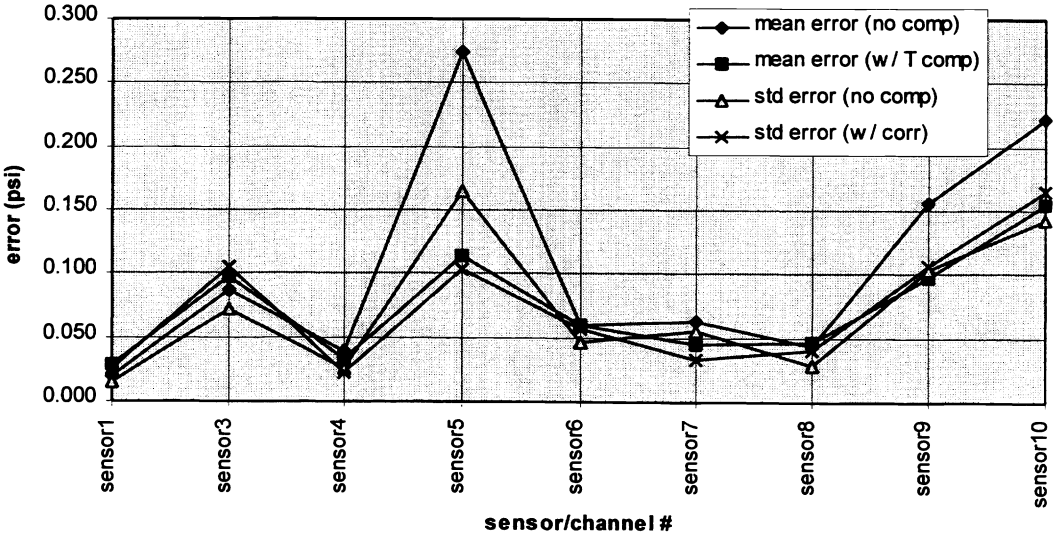

Figure 11. Observed pressure error vs. all channels.

values. In most cases the temperature corrected values were lower in error which indicated limited dependence upon temperature affects. Sensors 5, 9, and 10 showed a large error in the non-corrected values in addition to a large spread between the non-corrected mean and standard errors. This piece of information indicated that the output of these sensors was varying greatly from set to set. Temperature correcting these sensors improved the errors to less than 0.175 psi overall – the

observation that the final range after correction was not ~ 0.075 psi indicated that other effects were influencing the pressure output in those channels. The R2 values for these channels, when analyzed with respect to angle of attack, air velocity, or tunnel pressure, are much lower than that for temperature and probably can be ruled out as potential causes. Macrobending due to installation constraints was probably a leading cause in the values reported with sensors 5, 9, and 10.

5.2 Data presentation

The following four graphs are of temperature corrected data "snapshots" of runs in the TDT. The x-axis of each graph corresponds to a different angle of attack which accounts for the change in pressure from event 1 to event 12 while the y-axis shows the corresponding pressure scale. Additionally, the standard test profile was to set the tunnel wind speed and flap angle, and then adjust the angle of attack accordingly from some negative value through zero to a positive value. The data capture of each run typically ended with the angle of attack returning to zero as other parameters were varied. Due to the temperature correcting of these plots these graphs were adjusted so that the final data point corresponded to zero – note that this was purely an offset and not a scalar shift of the data. The data presented in Figure 12 shows a strong correlation between the F&S' fiber optic pressure sensor and its corresponding conventional pressure sensor and was typical for sensors 1, 3, 6, 7, and 8.

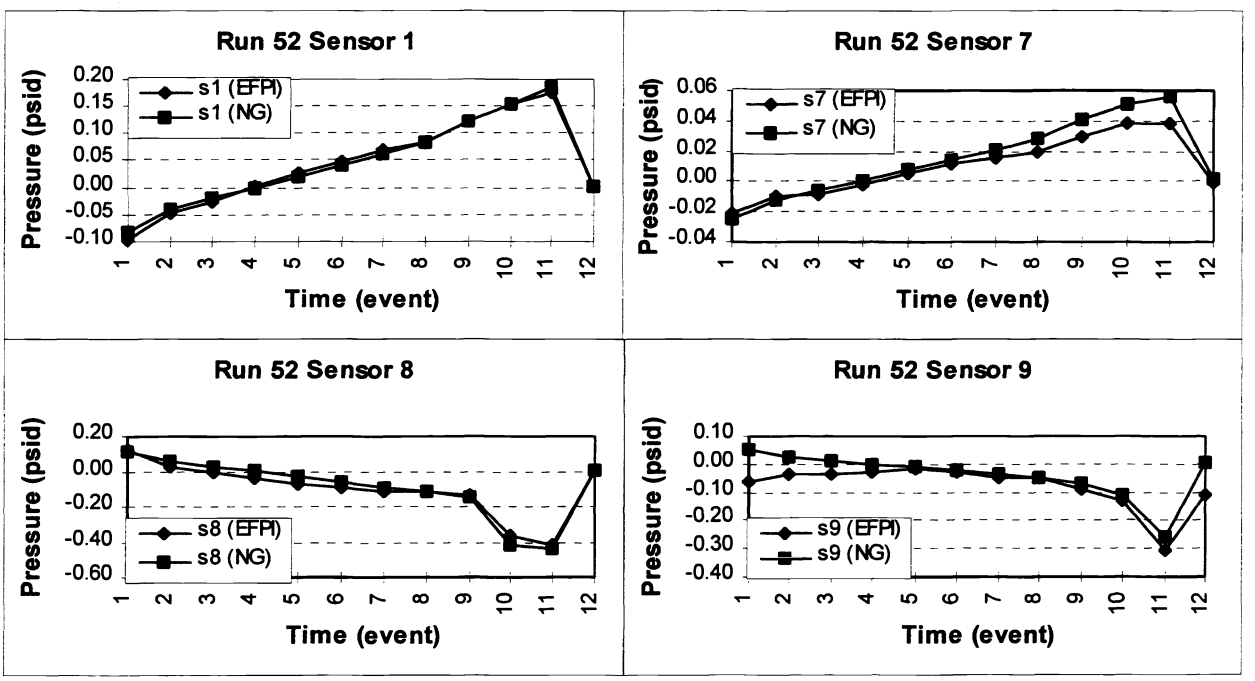

Figure 12. Plots of four channels for test run 52. The time (x-axis) scale corresponds to different angles of attack.

6. CONCLUSIONS

A new multi-channel fiber optic pressure system has been implemented to monitor air flow pressure over an adaptive wing. This system uses intensity modulation of a silicon diaphragm and principles based upon the extrinsic Fabry-Perot interferometer for demodulation. The fiber optic signal is conditioned and sampled at a high rate and processed by a DSP. The linearized pressure is output to a data acquisition system which stores the multi-channel data.

A temperature sensitivity in the fiber optic pressure sensors was observed which limited the mean accuracy to approximately 0.050 psi_d full-scale. Additionally, installation constraints caused bending losses which affected the sensor output. The mean accuracy could be dramatically improved by multiplexing a fiber optic temperature sensor at the tip of the pressure sensor and then performing the required calculations to correct the data. This multiplexing of fiber optic pressure and temperature sensors has already been successfully demonstrated at F&S and is being evaluated as a likely candidate for

the second phase of testing expected to begin in November, 1997. Issues surrounding the fiber clearance within the model were addressed at the first test and will be implemented during future testing.

ACKNOWLEDGEMENTS

The authors would like to thank the following people and organizations for their ongoing support of this and other related projects: Anna-Maria McGowan of NASA Langley, Jayanth Kudva and Christopher Martin of Northrop-Grumman Corporation, Doug Juanarena of Pressure Systems Incorporated, Mark West of Mission Research Corporation, and William Cockey, John Turman, Ryan Jones, and Ricky Crotts of F&S, Inc.

REFERENCES

[1] M. Di Giovanni, *Flat and Corrugated Diaphragm Design Handbook,* Marcel Dekker, New York, 1982

[2] K. Murphy, M. Gunther, A. Vengsarkar and R. O. Claus "Quadrature phase-shifted, extrinsic Fabry-Perot optical fiber sensors," *Optics Letters*, Vol. 16, No. 4, pp. 173-275, 1991.

[3] J.S. Milton and J.C. Arnold, *Introduction to Probability and Statistics*, pp. 403-408, McGraw-Hill, New York, 1990